

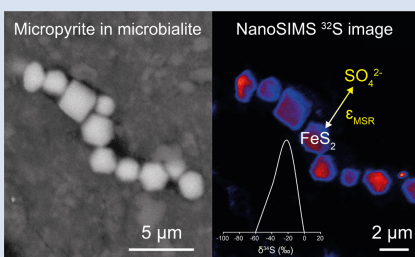
## Early precipitated micropyrite in microbialites: A time capsule of microbial sulfur cycling

J. Marin-Carbonne<sup>1\*</sup>, M.-N. Decraene<sup>1</sup>, R. Havas<sup>2</sup>, L. Remusat<sup>3</sup>, V. Pasquier<sup>4</sup>,  
J. Alléon<sup>1</sup>, N. Zeyen<sup>5</sup>, A. Bouton<sup>2</sup>, S. Bernard<sup>3</sup>, S. Escrig<sup>6</sup>, N. Olivier<sup>7</sup>,  
E. Vennin<sup>2</sup>, A. Meibom<sup>6,1</sup>, K. Benzerara<sup>3</sup>, C. Thomazo<sup>2,8</sup>



<https://doi.org/10.7185/geochemlet.2209>

### Abstract



Microbialites are organosedimentary rocks that have occurred throughout the Earth's history. The relationships between diverse microbial metabolic activities and isotopic signatures in biominerals forming within these microbialites are key to understanding modern biogeochemical cycles, but also for accurate interpretation of the geologic record. Here, we performed detailed mineralogical investigations coupled with NanoSIMS (Nanoscale Secondary Ion Mass Spectrometry) analyses of pyrite S isotopes in mineralising microbial mats from two different environments, a hypersaline lagoon (Cayo Coco, Cuba) and a volcanic alkaline crater lake (Atexcac, Mexico). Both microbialite samples contain two distinct pyrite morphologies: framboids and euhedral micropyrites, which display distinct ranges of  $\delta^{34}\text{S}$  values<sup>1</sup>. Considering

the sulfate-sulfur isotopic compositions associated with both environments, micropyrites display a remarkably narrow range of  $\Delta_{\text{pyr}}$  (*i.e.*  $\Delta_{\text{pyr}} \equiv \delta^{34}\text{S}_{\text{SO}_4} - \delta^{34}\text{S}_{\text{pyr}}$ ) between 56 and 62 ‰. These measured  $\Delta_{\text{pyr}}$  values agree with sulfate-sulfide equilibrium fractionation, as observed in natural settings characterised by low microbial sulfate reduction respiration rates. Moreover, the distribution of S isotope compositions recorded in the studied micropyrites suggests that sulfide oxidation also occurred at the microbialite scale. These results highlight the potential of micropyrites to capture signatures of microbial sulfur cycling and show that S isotope composition in pyrites record primarily the local micro-environments induced by the microbialite.

Received 21 October 2021 | Accepted 14 February 2022 | Published 21 March 2022

### Introduction

Sulfate-reducing bacteria, *i.e.* microorganisms that use sulfate as a terminal electron acceptor, are ubiquitous in Earth environments where they play a major role both in S and C biogeochemical cycles (*e.g.*, Jørgensen *et al.*, 2019). Microbial sulfate reduction (MSR) reduces sulfate to dissolved S species, such as HS<sup>-</sup> and H<sub>2</sub>S, and discriminates against heavy sulfur isotopes. The resulting sulfide  $\delta^{34}\text{S}$  values are relatively light and can be as much as -70 ‰ relative to sulfate (Jørgensen *et al.*, 2019). The fractionation induced by this metabolic activity (<sup>34</sup> $\epsilon_{\text{mic}}$  hereafter) depends on the sulfate concentration, identity of the electron donor, bioavailable carbon (content and chemical form) and, perhaps most importantly, the cell-specific sulfate reduction rates (csSRR; Bradley *et al.*, 2016). In modern environments, MSR can be identified by rate measurements with radiotracers or genomic and proteomic approaches. However, since genetic markers are

not preserved in the geological record, the recognition of MSR in palaeoenvironments mostly relies on the sulfur isotopic compositions of sedimentary sulfide and sulfate minerals (Visscher *et al.*, 2000; Fike *et al.*, 2008).

MSR plays a key role in carbonate mineralisation, especially identified in microbialites and microbial mats (Visscher *et al.*, 2000). Microbial mats are stratified microbial communities whose metabolic activities produce geochemical gradients and drive elemental cycling (Canfield and Des Marais, 1993; Paerl and Pinckney, 1996). In the geological record, such deposits (often referred to as stromatolites) are considered among the oldest trace of life on Earth (Allwood *et al.*, 2009). Some Archaean stromatolites contain carbonaceous laminae that have been interpreted as fossil microbial mats or biofilms based on textural evidence (Awramik, 1992; Lepot, 2020). Interestingly, determining the precise nature of the fossil microbial community

1. Institute of Earth Sciences, Université de Lausanne, Geopolis, Mouline 1015 Lausanne, Switzerland
2. UMR CNRS/UB6282 Biogéosciences, UFR Science Vie Terre Environnement, Université de Bourgogne Franche Comté, Dijon, France
3. Muséum National d'Histoire Naturelle, Sorbonne Université, CNRS UMR7590, Institut de Minéralogie, de Physique des Matériaux et de Cosmochimie (IMPMC), Paris, France
4. Earth and Planetary Sciences, Weizmann Institute of Sciences, Rehovot, Israel
5. Department of Earth and Atmospheric Sciences, University of Alberta, T6G 2E3, Canada
6. Laboratory for Biological Geochemistry, School of Architecture, Civil and Environmental Engineering, Ecole Polytechnique Fédérale de Lausanne, CH-1015 Lausanne, Switzerland
7. Université Clermont Auvergne, CNRS, IRD, Laboratoire Magmas et Volcans, F-63000 Clermont-Ferrand, France
8. Institut Universitaire de France, Paris, France

\* Corresponding author (email: [johanna.marincarbonne@unil.ch](mailto:johanna.marincarbonne@unil.ch))

<sup>1</sup> $\delta^{34}\text{S} = ((^{34}\text{S}/^{32}\text{S})_{\text{sample}} / (^{34}\text{S}/^{32}\text{S})_{\text{reference}} - 1) \times 1000$  in ‰, with Vienna Canyon Diablo Troilite as the reference.



is challenging because these organosedimentary rocks resulted from a complex balance between microbial activities, sedimentation and intermittent lithification (Reid *et al.*, 2000). In addition, the biosignatures preserved in fossil biofilms are ambiguous, especially after diagenesis and post-depositional history (Javaux, 2019; Alleon *et al.*, 2021). The oldest evidence for MSR in the Archaean geological record are sulfur isotopic signatures from deep marine sediments (Kamber and Whitehouse, 2007; Shen *et al.*, 2009) and stromatolites (Shen and Buick, 2004). In modern microbialites, numerous studies have reported dynamic MSR activity based on  $\text{H}_2\text{S}$  labelling (Visscher *et al.*, 2000; Fike *et al.*, 2008; Pace *et al.*, 2018; Gomes *et al.*, 2021), but only a few studies have investigated sulfur isotope signatures of individual pyrite grains (Gomes *et al.*, 2021).

The primary S isotopic signatures of pyrites ( $\text{FeS}_2$ ) are often modified by fluid circulation during metasomatism or metamorphism (Marin-Carbonne *et al.*, 2020; Slotznick *et al.*, 2022), occurring millions or billions of years after sediment deposition. While late diagenesis can modify both pyrite crystallinity and S isotope composition (Williford *et al.*, 2011; Gomes *et al.*, 2018; Marin-Carbonne *et al.*, 2020), early diagenesis in microbial mats is thought to have a limited effect on the S isotopic composition of pyrite, meaning that microbialitic pyrites may preserve 'pristine' isotopic signatures. However, the observation of large isotopic differences of about  $\sim 30\text{‰}$  (Raven *et al.*, 2016) between pore water sulfur species ( $\text{SO}_4^{2-}$  and  $\text{H}_2\text{S}$ ) and pyrite shows that other S-bearing pools, such as organic matter, should be considered in order to quantitatively and isotopically describe sulfur cycling in microbialites. Pyrite often precipitates at the microbial mat surface

(Gomes *et al.*, 2021) and its isotopic composition is more representative of the local setting rather than global environmental conditions, *e.g.*, water column (Lang *et al.*, 2020; Pasquier *et al.*, 2021). Decoding pyrite S isotopes at the micro-scale in sedimentary rocks is required to better understand how local conditions may affect the isotopic composition of microbialite pyrites. Here, we focus our investigation on two geographically independent modern microbial mats, which have not yet undergone (complete) lithification, and/or metasomatism.

## Syngenetic Microbialitic Pyrites

We studied two samples from 1) the Atexcac Lake, a monomictic volcanic crater lake (Mexico; Zeyen *et al.*, 2021) and 2) Cayo Coco Lake, a shallow hypersaline lagoon in Cuba (Pace *et al.*, 2018; Bouton *et al.*, 2020). These two depositional settings exhibit contrasting water column sulfate concentrations of 2.1 and 62 mM for Lake Atexcac and Cayo Coco, respectively (Figs. S-1 and S-2, SI). Both samples were produced by mineralising microbial mats and contained authigenic aragonite, Mg-rich calcite, dolomite, authigenic hydrated Mg-silicates/silica such as kerolite, and detrital phases such as feldspars and illite (Figs S-1 and S-2, SI). In each locality, pyrite morphologies fall into two different categories (Fig. 1): framboidal pyrites, ranging from 3 to 15  $\mu\text{m}$ , and mono-crystal pyrites of a few micrometres ( $>3\ \mu\text{m}$ ), hereafter called micropyrates (Figs. 1 and 2, SI). Transmission electron microscopy analyses revealed an early origin of the micropyrates grains (SI). Considering both the

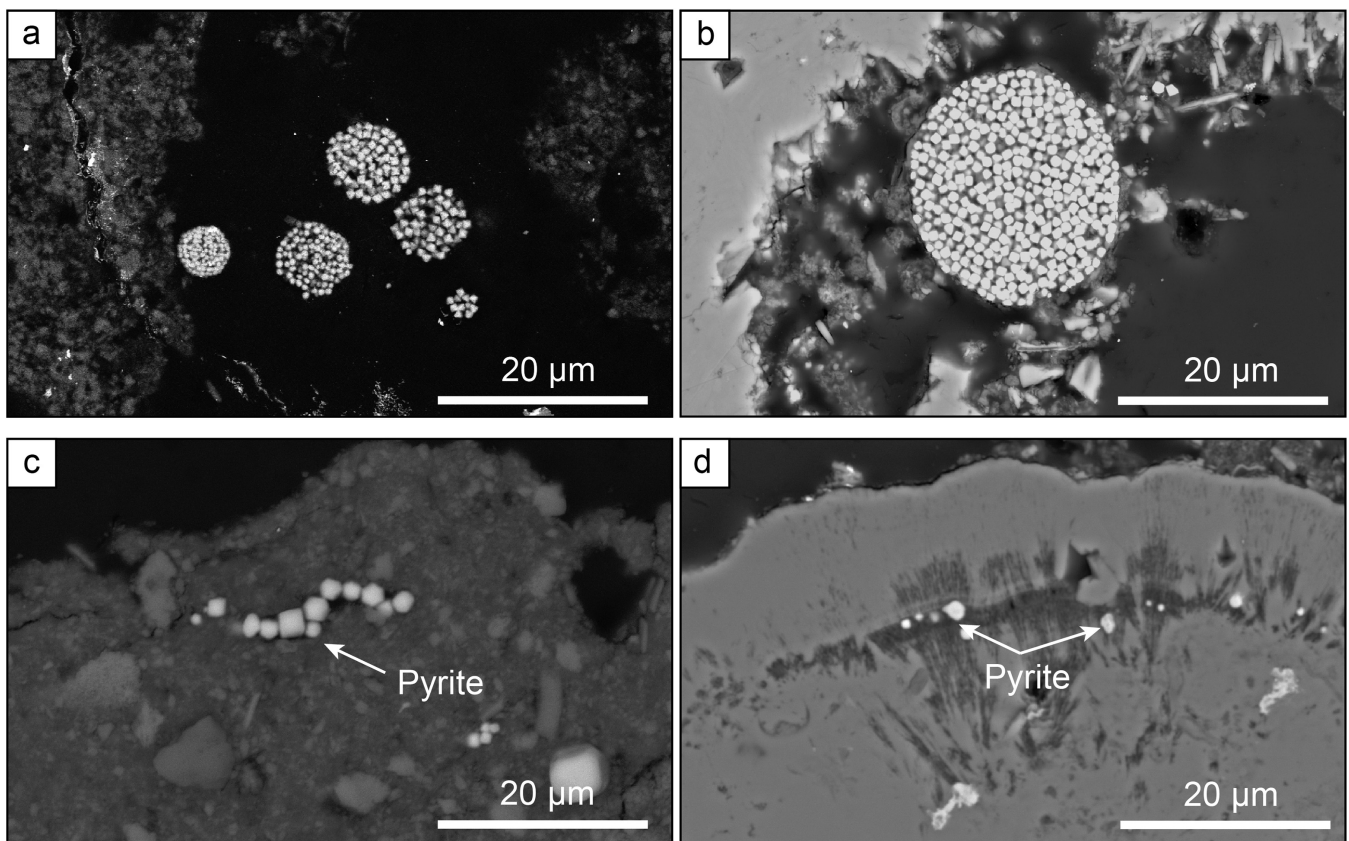


**Figure 1** Secondary Electron microscopy pictures of (a, b) framboidal pyrites and (c, d) micropyrates from (a, c) Cayo Coco Lagoon and (b, d) Atexcac. Framboidal pyrites are located at the surface of the mineralised microbialite (in dark) while micropyrates are entombed within aragonite (in light grey) or Mg rich silicate (dark grey).

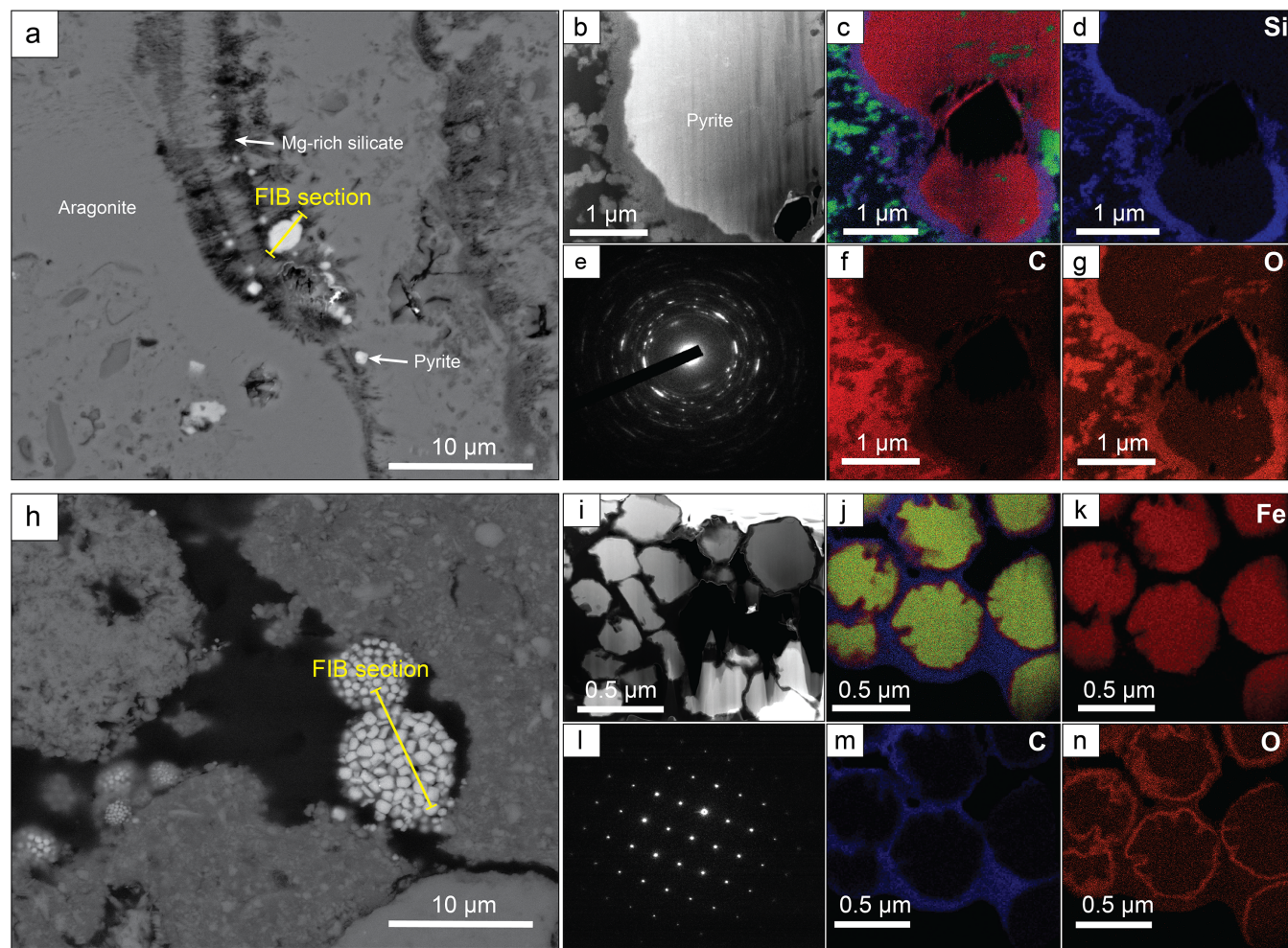


**Figure 2** (a) SEM picture of micropyrates. Location where FIB section was extracted is shown by the yellow line, (b) TEM picture of the pyrite crystal and (e) its associated powder-like diffraction pattern, (c) false colour STEM EDXS image (Si in blue, Ca in green, Fe in red) and (d, f, g) Si, C and O images of the submicrometric pyrites, respectively. (h) SEM picture of framboidal pyrite with FIB section location (yellow line), (i) TEM image and (l) associated single crystal diffraction pattern along the [112] zone axis of pyrite, (j) false colour STEM EDXS image of pyrite crystallites (Fe in red, S in green, C in blue) and (k, m, n) Fe, C and O images, respectively.

alignment of the micropyrates within the organic lamination and their crystallinity, micropyrates are likely formed during an early lithification stage (SI).

### NanoSIMS S Isotope Composition of Pyrites

The S isotope compositions of 66 framboidal pyrites and 55 individual micropyrates were measured by NanoSIMS with a reproducibility better than 2‰ ( $2\sigma$ , see SI). Framboidal pyrites display a  $\sim 20$ – $30$ ‰ range in  $\delta^{34}\text{S}$  values with an average of  $-26.1 \pm 7$ ‰ and  $-26.4 \pm 9$ ‰ (2 s.d.) for Atexcac and Cayo Coco, respectively (Figs. 3 and 4). We have extracted S isotope composition of individual crystallites from four framboids (Fig. 3, SI). All framboidal pyrites ( $n = 4$ ) show a large internal  $\delta^{34}\text{S}$  variability ( $\sim 40$ ‰, Fig. 3) characterised by a gradient from  $\sim +8.5 \pm 1.5$ ‰ to more  $^{34}\text{S}$ -depleted values ranging from  $-42$  to  $-69$ ‰. Micropyrates also show large S isotope heterogeneities with  $\delta^{34}\text{S}$  values ranging from  $-86$  to  $-17$ ‰ with an average value of  $-61.4 \pm 17$ ‰ for Atexcac, and from  $-53$  to  $-21$ ‰ with an average value of  $-34.5 \pm 29$ ‰ in Cayo Coco (Fig. 4).

### Framboidal Pyrites Record a Mixing of Reduction and Oxidation Processes

Framboidal pyrites display a large range of  $\delta^{34}\text{S}$  values but also an internal isotope variation across the length scale of individual framboidal grains (Fig. 3), best explained by a combination of MSR and partial sulfide oxidation (Fig. 3; Pellerin *et al.*, 2019). As framboidal pyrites are mostly observed at the surface of the mat, S isotope variations reflect the mixing of in situ production, upward diffusion of sulfide in the mat and its subsequent reoxidation at the mat surface. The fractionation required to produce such an isotopic gradient is well above abiotic sulfide oxidation (*i.e.*  $\sim +5$ ‰; Fry *et al.*, 1988), yet can also be consistent with microbial sulfide oxidation in high pH environments (Pellerin *et al.*, 2019). Both sites are characterised by high pH ( $\text{pH} > 8$ , see SI), which is known to promote large isotope fractionation during sulfide oxidation (Pellerin *et al.*, 2019). Consequently, part of the observed range of  $\delta^{34}\text{S}$  values may be attributed to local variation of S speciation associated with pH. As such, the internal gradient may be the result of microbially mediated surface  $\text{H}_2\text{S}$  oxidation. Alternatively, the internal isotope gradient across the framboidal pyrites (Fig. 2, SI) can be due to Rayleigh isotope fractionation, as even under

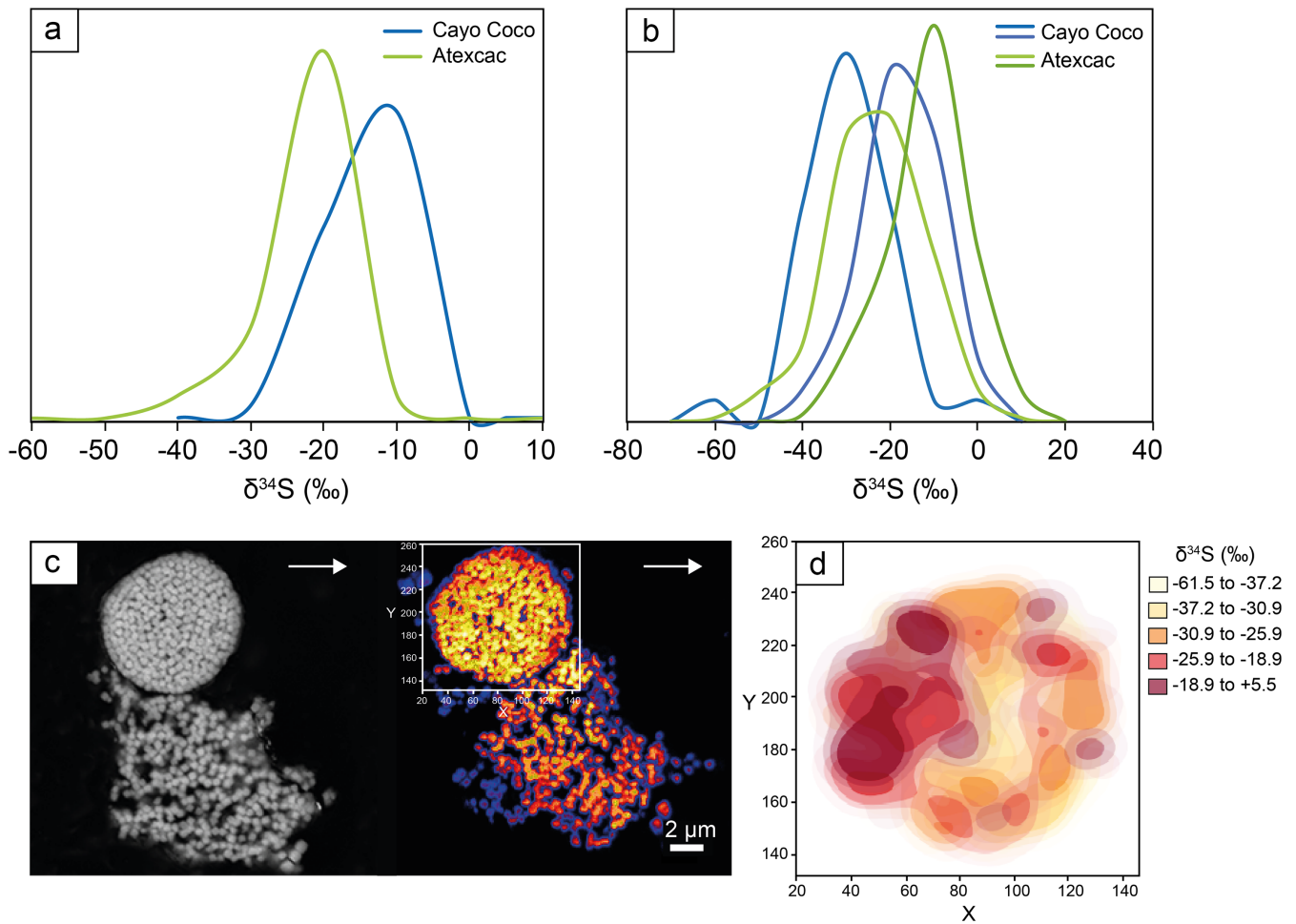


**Figure 3** (a)  $\delta^{34}\text{S}$  probability density function of all framboidal pyrites from Atexcac and Cayo Coco uncertainties of analyses ranges from 0.4 to 4 ‰, (b)  $\delta^{34}\text{S}$  probability density function of four individual framboidal pyrites containing up to 100 pyrite crystallites, (c) SEM and corresponding NanoSIMS  $^{32}\text{S}$  image of one framboidal pyrite; the arrow indicates the top of the mat, and (d)  $\delta^{34}\text{S}$  values reconstructed for individual pyrite crystallites showing strong variations in S isotope composition across the framboidal pyrite.

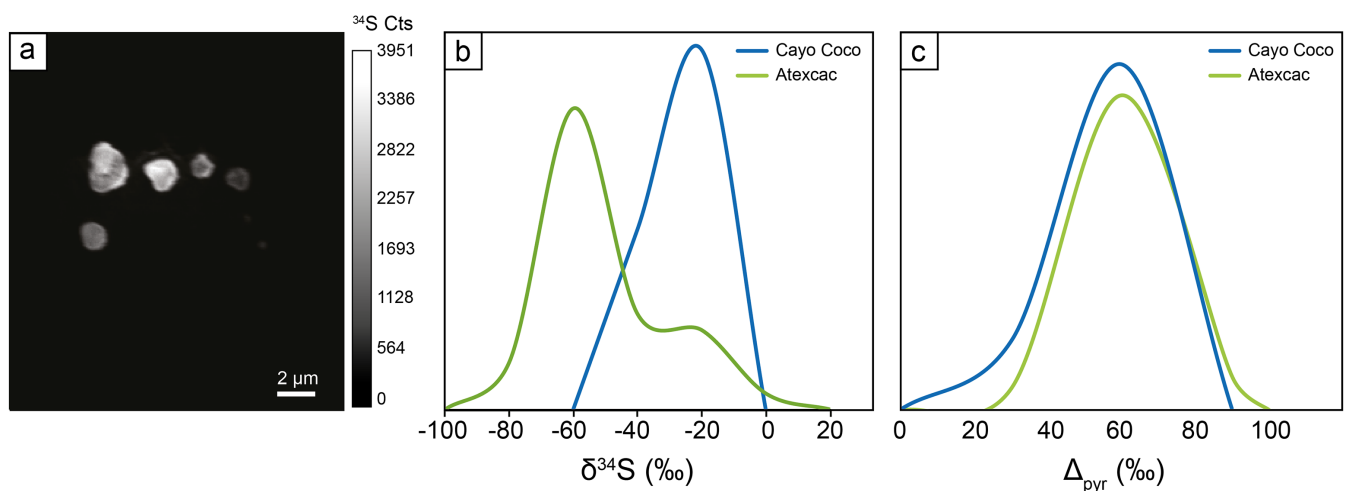


**Figure 4** (a) NanoSIMS  $^{32}\text{S}$  image of submicrometric pyrites, (b)  $\delta^{34}\text{S}$  probability density function, taking account of the range of uncertainties from 1 ‰ to 8 ‰ of micropyrites from Cayo Coco and Atexcac, (c)  $\Delta_{\text{pyr}}$  distribution calculated for both environments.

oxidising (abundant sulfate) conditions, consumption can occur faster than diffusive replenishment (Goldhaber and Kaplan, 1980). Rather than reflecting water column conditions, the S

isotope composition of framboidal pyrites appears to be strongly influenced by local redox conditions (*i.e.* at the microbial mat scale).

## Microbialitic Micropyrrite Preserve Primary Isotopic Microbial Fractionation Signatures

The presence of Mg silicate rich rims (SI) suggests that micropyrrites were probably formed very early during lithification (Fig. 2). Moreover, the small crystal size of micropyrrites composed of nanocrystals with different orientations has been highlighted as a possible biogenic signature (Picard *et al.*, 2018). The  $\delta^{34}\text{S}$  values of dissolved sulfate are +0.52 ‰ in Atexcac and are assumed to be close to seawater composition (+21 ‰) for Cayo Coco (SI). Considering these hugely contrasting isotopic compositions of sulfate, micropyrrites display surprisingly similar  $\Delta_{\text{pyr}}$  values (*i.e.*  $\Delta_{\text{pyr}} = \delta^{34}\text{S}_{\text{SO}_4} - \delta^{34}\text{S}_{\text{pyr}}$ ) of  $62 \pm 17$  ‰ and  $56 \pm 29$  ‰ for Atexcac and Cayo Coco, respectively (Fig. 4). These  $\Delta_{\text{pyr}}$  values are consistent with near thermodynamic equilibrium fractionation as observed in *i)* MSR batch culture experiments characterised by low growth rate and csSRR (Leavitt *et al.*, 2013; Bradley *et al.*, 2016) and *ii)* natural environments (*e.g.*, Cadagno Lake; Canfield *et al.*, 2010). High  $^{34}\text{S}_{\text{mic}}$  has been observed in sulfate reducing strains only partially oxidising their carbon substrate and is sometimes associated with the degradation of carbohydrate components, including exopolymeric substances (EPS) (Sim *et al.*, 2011), which are abundant in microbialite-forming mats. Atexcac waters have a high dissolved organic carbon content (over 15 times that of the modern ocean) which can sustain MSR activity, while Cayo Coco harbours conspicuous suspended EPS-rich organic slimes (Bouton *et al.*, 2016). Despite abundant sulfate (at Cayo Coco) and organic matter, csSRR in these mats are intriguingly low and contrast with previous occurrences of high SRR in surface microbial mats (Canfield and Des Marais, 1993). Low csSRR and high S isotope fractionations in both lakes could be explained by the refractory nature of this organic matter (Bouton *et al.*, 2020; Gomes *et al.*, 2021). At the microbial mat scale, strong gradients of sulfate reduction within layered mats (Visscher *et al.*, 2000; Fike *et al.*, 2009; Pace *et al.*, 2018) have been attributed to small scale variations in csSRR and/or localised MSR micro-niches (Fike *et al.*, 2009; Gomes *et al.*, 2021). The observed laminations, which contain micropyrrites, likely reflect local high density microbe spots, which can result from a more pronounced local distillation of  $\delta^{34}\text{S}$  (Pasquier *et al.*, 2021). Alternatively, the composition of microbial consortia may affect the range of csSRR at the microbial mat scale (Bradley *et al.*, 2016), with guild diversity having opposite effects on trophic group functions, thus modulating csSRR (Bell *et al.*, 2005; Peter *et al.*, 2011).

## Conclusions

Here, we have shown that the S isotope composition of fram-boids and micropyrrites reflects sulfur cycling at the scale of the mat environment. While S isotope signatures in microbialite micropyrrites are primarily controlled by MSR, they can also be influenced by oxidative sulfur cycling in high pH environments. Notably, microbialites growing at different dissolved sulfate concentrations and in marine versus lacustrine environments display similar micropyrrite morphologies and comparable  $\Delta_{\text{pyr}}$ . Such observations demonstrate that microbialites have the potential to record the isotopic fractionation associated with MSR irrespective of the depositional environment and sulfate level. Consequently, we propose that microbialite micropyrrites can be used as a mineral signature for reconstructing past Earth surface and microbial environments, as already suggested for Archaeal stromatolites (Marin-Carbonne *et al.*, 2018). In addition, this study clearly shows that caution should be used

in reconstructing past environmental parameters, such as water body sulfate levels, from  $\Delta_{\text{pyr}}$ . Finally, the respective influence of different electron donors, sulfate concentration, and non-actualistic microbial communities on the csSRR and associated sedimentary pyrites  $\delta^{34}\text{S}$  remains to be explored in order to deepen our understanding of the evolutionary trajectory of biogeochemical sulfur cycling on Earth.

## Author contributions

JMC, LR, SB and CT designed the study, KB, EV, CT and AB collected samples in the field. JMC, LR, MND and SE conducted the NanoSIMS analyses, CT and RH conducted the bulk S isotope analyses. JMC, MND, JA, AB, NZ and KB conducted the microscope observations. All authors have contributed to the data interpretation. JMC wrote the manuscript with important contributions of all co-authors.

## Competing interests

Authors declare no competing interests.

## Data and materials availability

All data is available in the main text or the supplementary materials.

## Additional Information

Supplementary Information accompanies this letter at <https://www.geochemicalperspectivesletters.org/article2209>.

## Acknowledgements

This research was supported through the European Research council (ERC) under the European Union's Horizon H2020 research and innovation programme (STROMATA grant agreement 759289). The NanoSIMS facility at the Museum National d'Histoire Naturelle in Paris was established by funds from the CNRS, region ile de France, Ministère délégué à l'enseignement et à la recherche and the Museum National d'Histoire Naturelle. We thank Kevin McKeegan and Jasmine Berg for their proof-reading of the manuscript and for fruitful discussions.

Editor: Tanja Bosak



© 2022 The Authors. This work is distributed under the Creative Commons Attribution Non-Commercial No-Derivatives 4.0

License, which permits unrestricted distribution provided the original author and source are credited. The material may not be adapted (remixed, transformed or built upon) or used for commercial purposes without written permission from the author. Additional information is available at <https://www.geochemicalperspectivesletters.org/copyright-and-permissions>.

**Cite this letter as:** Marin-Carbonne, J., Decraene, M.-N., Havas, R., Remusat, L., Pasquier, V., Alléon, J., Zeyen, N., Bouton, A., Bernard, S., Escrig, S., Olivier, N., Vennin, E., Meibom, A., Benzerara, K., Thomazo, C. (2022) Early precipitated micropyrrite in microbialites: A time capsule of microbial sulfur cycling. *Geochem. Persp. Let.* 21, 7–12. <https://doi.org/10.7185/geochemlet.2209>



## References

- ALLEON, J., BERNARD, S., OLIVIER, N., THOMAZO, C., MARIN-CARBONNE, J. (2021) Inherited geochemical diversity of 3.4 Ga organic films from the Buck Reef Chert, South Africa. *Communications Earth & Environment* 2, 6. <https://doi.org/10.1038/s43247-020-00066-7>
- ALLWOOD, A.C., GROTZINGER, J.P., KNOLL, A.H., BURCH, I.W., ANDERSON, M.S., COLEMAN, M.L., KANIK, I. (2009) Controls on development and diversity of Early Archean stromatolites. *Proceedings of the National Academy of Sciences* 106, 9548–9555. <https://doi.org/10.1073/pnas.0903323106>
- AWRAMIK, S.M. (1992) The history and significance of stromatolite. In: SCHIDLÓWSKI, M., GOLUBIC, S., KIMBERLEY, M.M., MCKIRDY, D.M., TRUDINGER, P.A. (Eds.) *Early organic evolution*. Springer, Berlin, 435–449. [https://doi.org/10.1007/978-3-642-76884-2\\_34](https://doi.org/10.1007/978-3-642-76884-2_34)
- BELL, T., NEWMAN, J.A., SILVERMAN, B.W., TURNER, S.L., LILLEY, A.K. (2005) The contribution of species richness and composition to bacterial services. *Nature* 436, 1157–1160. <https://doi.org/10.1038/nature03891>
- BOUTON, A., VENNIN, E., PACE, A., BOURILLOT, R., DUPRAZ, C., THOMAZO, C., BRAYARD, A., DÉSAUBLAUX, G., VISSCHER, P.T. (2016) External controls on the distribution, fabrics and mineralization of modern microbial mats in a coastal hypersaline lagoon, Cayo Coco (Cuba). *Sedimentology* 63, 972–1016. <https://doi.org/10.1111/sed.12246>
- BOUTON, A., VENNIN, E., THOMAZO, C., MATHIEU, O., GARCIA, F., JAUBERT, M., VISSCHER, P. (2020) Microbial Origin of the Organic Matter Preserved in the Cayo Coco Lagoonal Network, Cuba. *Minerals* 10, 143. <https://doi.org/10.3390/min10020143>
- BRADLEY, A.S., LEAVITT, W.D., SCHMIDT, M., KNOLL, A.H., GIRGIS, P.R., JOHNSTON, D.T. (2016) Patterns of sulfur isotope fractionation during microbial sulfate reduction. *Geobiology* 14, 91–101. <https://doi.org/10.1111/gbi.12149>
- CANFIELD, D.E., DES MARAIS, D.J. (1993) Biogeochemical cycles of carbon, sulfur, and free oxygen in a microbial mat. *Geochimica et Cosmochimica Acta* 57, 3971–3984. [https://doi.org/10.1016/0016-7037\(93\)90347-Y](https://doi.org/10.1016/0016-7037(93)90347-Y)
- CANFIELD, D.E., FARQUHAR, J., ZERKLE, A.L. (2010) High isotope fractionations during sulfate reduction in a low-sulfate euxinic ocean analog. *Geology* 38, 415–418. <https://doi.org/10.1130/G30723.1>
- FIKE, D.A., FINKE, N., ZHA, J., BLAKE, G., HOEHLER, T.M., ORPHAN, V.J. (2009) The effect of sulfite concentration on (sub)millimeter-scale sulfide  $\delta^{34}\text{S}$  in hypersaline cyanobacterial mats over the diurnal cycle. *Geochimica et Cosmochimica Acta* 73, 6187–6204. <https://doi.org/10.1016/j.gca.2009.07.006>
- FIKE, D.A., GAMMON, C.L., ZIEBIS, W., ORPHAN, V.J. (2008) Micron-scale mapping of sulfur cycling across the oxycline of a cyanobacterial mat: a paired nanoSIMS and CARD-FISH approach. *The ISME Journal* 2, 749–759. <https://doi.org/10.1038/ismej.2008.39>
- FRY, B., RUE, W., GEST, H., HAYES, J.M. (1988) Sulfur isotope effects associated with oxidation of sulfide by  $\text{O}_2$  in aqueous solution. *Chemical Geology: Isotope Geoscience section* 73, 205–210. [https://doi.org/10.1016/0168-9622\(88\)90001-2](https://doi.org/10.1016/0168-9622(88)90001-2)
- GOLDBABER, M.B., KAPLAN, I.R. (1980) Mechanisms of sulfur incorporation and isotope fractionation during early diagenesis in sediments of the Gulf of California. *Marine Chemistry* 9, 95–143. [https://doi.org/10.1016/0304-4203\(80\)90063-8](https://doi.org/10.1016/0304-4203(80)90063-8)
- GOMES, M.L., FIKE, D.A., BERGMANN, K.D., JONES, C., KNOLL, A.H. (2018) Environmental insights from high-resolution (SIMS) sulfur isotope analyses of sulfides in Proterozoic microbialites with diverse mat textures. *Geobiology* 16, 17–34. <https://doi.org/10.1111/gbi.12265>
- GOMES, M.L., KLATT, J.M., DICK, G.J., GRIM, S.L., RICO, K.I., MEDINA, M., ZIEBIS, W., KINSMAN-COSTELLO, L., SHELDON, N.D., FIKE, D.A. (2021) Sedimentary pyrite sulfur isotope compositions preserve signatures of the surface microbial mat environment in sediments underlying low-oxygen cyanobacterial mats. *Geobiology* 20, 60–78. <https://doi.org/10.1111/gbi.12466>
- JAVAUX, E.J. (2019) Challenges in evidencing the earliest traces of life. *Nature* 572, 451–460. <https://doi.org/10.1038/s41586-019-1436-4>
- JØRGENSEN, B.B., FINDLAY, A.J., PALLERIN, A. (2019) The Biogeochemical Sulfur Cycle of Marine Sediments. *Frontiers in Microbiology* 10, 849. <https://doi.org/10.3389/fmicb.2019.00849>
- KAMBER, B.S., WHITEHOUSE, M.J. (2007) Micro-scale sulphur isotope evidence for sulphur cycling in the late Archean shallow ocean. *Geobiology* 5, 5–17. <https://doi.org/10.1111/j.1472-4669.2006.00091.x>
- LANG, X., TANG, W., MA, H., SHEN, B. (2020) Local environmental variation obscures the interpretation of pyrite sulfur isotope records. *Earth and Planetary Science Letters* 533, 116056. <https://doi.org/10.1016/j.epsl.2019.116056>
- LEAVITT, W.D., HALEVY, I., BRADLEY, A.S., JOHNSTON, D.T. (2013) Influence of sulfate reduction rates on the Phanerozoic sulfur isotope record. *Proceedings of the National Academy of Sciences* 110, 11244–11249. <https://doi.org/10.1073/pnas.1218874110>
- LEPOT, K. (2020) Signatures of early microbial life from the Archean (4 to 2.5 Ga) eon. *Earth-Science Reviews* 209, 103296. <https://doi.org/10.1016/j.earscirev.2020.103296>
- MARIN-CARBONNE, J., BUSIGNY, V., MIOT, J., ROLLION-BARD, C., MULLER, E., DRABON, N., JACOB, D., PONT, S., ROBYR, M., BONTIGNALI, T.R.R., FRANÇOIS, C., REYNAUD, S., VAN ZUILEN, M., PHILIPPOT, P. (2020) In Situ Fe and S isotope analyses in pyrite from the 3.2 Ga Mendon Formation (Barberton Greenstone Belt, South Africa): Evidence for early microbial iron reduction. *Geobiology* 18, 306–325. <https://doi.org/10.1111/gbi.12385>
- MARIN-CARBONNE, J., REMUSAT, L., SFORNA, M.C., THOMAZO, C., CARTIGNY, P., PHILIPPOT, P. (2018) Sulfur isotope's signal of nanopyrates enclosed in 2.7 Ga stromatolitic organic remains reveal microbial sulfate reduction. *Geobiology* 16, 121–138. <https://doi.org/10.1111/gbi.12275>
- PACE, A., BOURILLOT, R., BOUTON, A., VENNIN, E., BRAISSANT, O., DUPRAZ, C., DUTEL, T., BUNDELEVA, I., PATRIER, P., GALAUP, S., YOKOYAMA, Y., FRANCESCHI, M., VIRGONE, A., VISSCHER, P.T. (2018) Formation of stromatolite lamina at the interface of oxygenic-anoxygenic photosynthesis. *Geobiology* 16, 378–398. <https://doi.org/10.1111/gbi.12281>
- PAERL, H.W., PINCKNEY, J.L. (1996) A mini-review of microbial consortia: their roles in aquatic production and biogeochemical cycling. *Microbial Ecology* 31, 225–247. <https://doi.org/10.1007/BF00171569>
- PASQUIER, V., BRYANT, R.N., FIKE, D.A., HALEVY, I. (2021) Strong local, not global, controls on marine pyrite sulfur isotopes. *Science Advances* 7, eabb7403. <https://doi.org/10.1126/sciadv.abb7403>
- PELLERIN, A., ANTLER, G., HOLM, S.A., FINDLAY, A.J., CROCKFORD, P.W., TURCHYN, A.V., JØRGENSEN, B.B., FINSTER, K. (2019) Large sulfur isotope fractionation by bacterial sulfide oxidation. *Science Advances* 5, eaaw1480. <https://doi.org/10.1126/sciadv.aaw1480>
- PETER, H., BEIER, S., BERTILSSON, S., LINDSTRÖM, E.S., LANGENHEDER, S., TRANVIK, L.J. (2011) Function-specific response to depletion of microbial diversity. *The ISME Journal* 5, 351–361. <https://doi.org/10.1038/ismej.2010.119>
- PICARD, A., GARTMAN, A., CLARKE, D.R., GIRGIS, P.R. (2018) Sulfate-reducing bacteria influence the nucleation and growth of mackinawite and greigite. *Geochimica et Cosmochimica Acta* 220, 367–384. <https://doi.org/10.1016/j.gca.2017.10.006>
- RAVEN, M.R., SESSIONS, A.L., FISCHER, W.W., ADKINS, J.F. (2016) Sedimentary pyrite  $\delta^{34}\text{S}$  differs from porewater sulfide in Santa Barbara Basin: Proposed role of organic sulfur. *Geochimica et Cosmochimica Acta* 186, 120–134. <https://doi.org/10.1016/j.gca.2016.04.037>
- REID, R.P., VISSCHER, P.T., DECHO, A.W., STOLZ, J.F., BEBOUT, B.M., DUPRAZ, C., MACINTYRE, I.G., PAERL, H.W., PINCKNEY, J.L., PRUFERT-BEBOUT, J., STEPPE, T.F., DESMARAIS, D.J. (2000) The role of microbes in accretion, lamination and early lithification of modern marine stromatolites. *Nature* 406, 989–992. <https://doi.org/10.1038/35023158>
- SHEN, Y., FARQUHAR, J., MASTERTON, A., KAUFMAN, A.J., BUICK, R. (2009) Evaluating the role of microbial sulfate reduction in the early Archean using quadruple isotope systematics. *Earth and Planetary Science Letters* 279, 383–391. <https://doi.org/10.1016/j.epsl.2009.01.018>
- SHEN, Y., BUICK, R. (2004) The antiquity of microbial sulfate reduction. *Earth-Science Reviews* 64, 243–272. [https://doi.org/10.1016/S0012-8252\(03\)00054-0](https://doi.org/10.1016/S0012-8252(03)00054-0)
- SIM, M.S., ONO, S., DONOVAN, K., TEMPLER, S.P., BOSAK, T. (2011) Effect of electron donors on the fractionation of sulfur isotopes by a marine *Desulfovibrio* sp. *Geochimica et Cosmochimica Acta* 75, 4244–4259. <https://doi.org/10.1016/j.gca.2011.05.021>
- SLOTZNICK, S.P., JOHNSON, J.E., RASMUSSEN, B., RAUB, T.D., WEBB, S.M., ZI, J.-W., KIRSCHVINK, J.L., FISCHER, W.W. (2022) Reexamination of 2.5-Ga “whiff” of oxygen interval points to anoxic ocean before GOE. *Science Advances* 8, eabj7190. <https://doi.org/10.1126/sciadv.abj7190>
- VISSCHER, P.T., REID, R.P., BEBOUT, B.M. (2000) Microscale observations of sulfate reduction: Correlation of microbial activity with lithified micritic laminae in modern marine stromatolites. *Geology* 28, 919–922. [https://doi.org/10.1130/0091-7613\(2000\)28<919:MOOSRC>2.0.CO;2](https://doi.org/10.1130/0091-7613(2000)28<919:MOOSRC>2.0.CO;2)
- WILLIFORD, K.H., VAN KRANENDONK, M.J., USHIKUBO, T., KOZDON, R., VALLEY, J.W. (2011) Constraining atmospheric oxygen and seawater sulfate concentrations during Paleoproterozoic glaciation: In situ sulfur three-isotope microanalysis of pyrite from the Turee Creek Group, Western Australia. *Geochimica et Cosmochimica Acta* 75, 5686–5705. <https://doi.org/10.1016/j.gca.2011.07.010>
- ZEVEN, N., BENZERARA, K., BEYSSAC, O., DAVAL, D., MULLER, E., THOMAZO, C., TAVERA, R., LÓPEZ-GARCÍA, P., MOREIRA, D., DUPRAT, E. (2021) Integrative analysis of the mineralogical and chemical composition of modern microbialites from ten Mexican lakes: What do we learn about their formation. *Geochimica et Cosmochimica Acta* 305, 148–184. <https://doi.org/10.1016/j.gca.2021.04.030>



## Early precipitated micropyrrite in microbialites: A capsule of microbial sulfur cycling

**J. Marin-Carbonne, M.-N. Decraene, R. Havas, L. Remusat, V. Pasquier, J. Alleon, N. Zeyen, A. Bouton, N. Olivier, S. Escrig, E. Vennin, A. Meibom, K. Benzerara, C. Thomazo**

### Supplementary Information

The Supplementary Information includes:

- Sample Descriptions
- Methods
- Framboidal Pyrites
- Tables S-1 to S-5
- Figures S-1 to S-10
- Supplementary Information References

### Sample Descriptions

#### Atexcac Microbialite

The studied sample (ATX-2012-08) consists of a microbialite collected at about 0.1 m below the lake water level (Zeyen *et al.*, 2015) in January 2012. Atexcac is a maar lake covering an area of 27 ha, located in the eastern part of the trans-Mexican volcanic belt in the Cuenca de Oriental basin (Puebla State), in the Los Llanos de San Juan region. The salinity of Lake Atexcac varies between 7 and 8 g L<sup>-1</sup>, pH is around 8.5 and average temperature is 18.3 °C (Sigala *et al.*, 2017; Zeyen *et al.*, 2021). The studied sample (ATX-2012-08) was collected on the Southwestern shore of the lake (Fig. S-1). The mineralogy of the sample consists of aragonite and authigenic silicates, likely kerolite and/or stevensite.

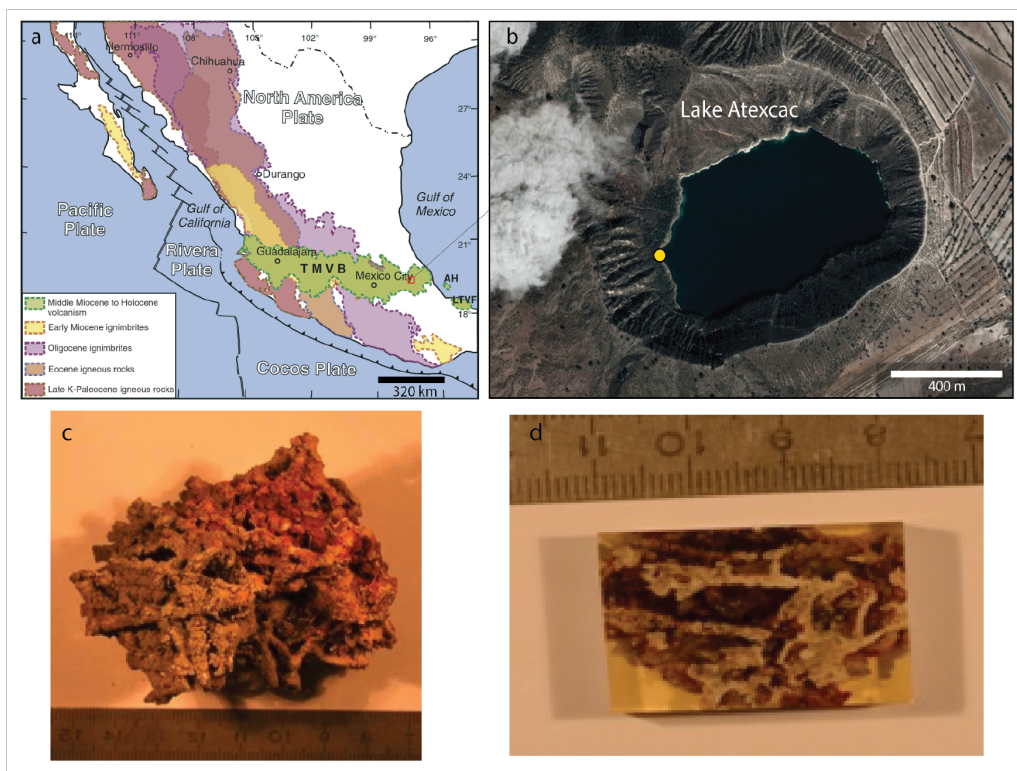


**Figure S-1** Geographic location of Lake Atexcac. **(a)** Geological map representing the location of the trans-Mexican volcanic belt (TMVB, green area) from Ferrari *et al.* (2012) and the location of Lake Atexcac marked by a red square. **(b)** Google Earth image of the lake. The yellow circle corresponds to the microbialite sampling area in January 2012. **(c)** Close view of the sample and **(d)** sample included in epoxy.

### Cayo Coco Microbialite

Hypersaline Cayo Coco lagoonal network is located on the south side of the island of Cayo Coco on the Atlantic coast of Cuba and consists of partially connected shallow lagoons related to the Caribbean sea through the Perros Bay. Eastern lagoon consists of wide variety of mineralising microbial mats and few microbialites (Bouton *et al.*, 2016; Pace *et al.*, 2018). This lagoon is disconnected from the rest of the network by a 50 m wide bioclastic sands and is 1 km long and 600 m wide with a maximum water depth of 75 cm. The salinity of the lagoon varying seasonably from 54 ‰ to 75 ‰, pH varying from 8 to 9, average temperature is 25.8 °C (Cepero and Lawrence, 2006; Gonzalez-De Zayas and Merino-Ibarra, 2010; Bouton *et al.*, 2020;). This lagoon is characterised by an evaporation range between 2100 and 2200 mm and limited exchange with the ocean (Gonzalez-De Zayas and Merino-Ibarra, 2010).

The sample (M2, 6.8–7.1 cm deep) studied there come from the microbial flat depositional environment from the west transect of the submersed lagoon (Fig. S-2; Bouton *et al.*, 2020). The mineralised microbial mat has been selected from the core CC2 investigated in detail by Bouton *et al.* (2020). The sample consists of microbial mat fragment embedded in a micritic mud containing bioclastic fragments (*i.e.* foraminifera, bivalves and gastropods). The fragment is similar in composition to the mineralising microbial mat observed on the shore. The mat is still composed of several lamina (an upper green indicative of ancient filamentous cyanobacterial communities and below, a brown to black lamina depicting the presence of FeS and resulting from anaerobic heterotrophic metabolism, especially sulfate-reducing bacteria (SRB) with a mm-thick carbonate crust. The presence of relics of mineralising microbial mats preserved in micritic mud is related to fluctuations in the water level over time. The mineralogy of the sample consists of high magnesium calcite, Mg silicate, aragonite, detrital grains, foraminifera tests and sulfides.

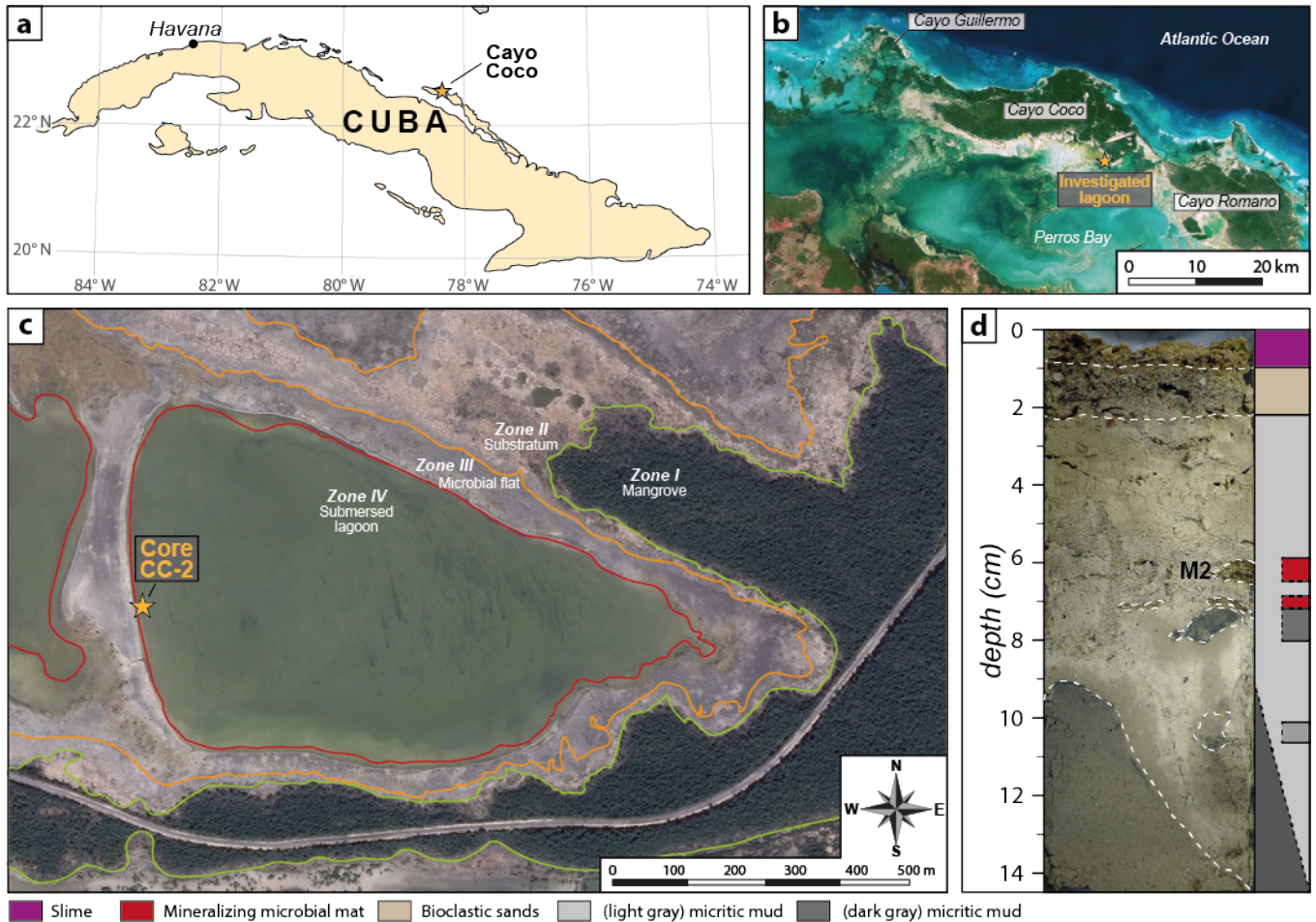


**Figure S-2** Sampling location at Cayo Coco Lagoon. **(a)** Cuba map with the location of Cayo Coco Lagoon (star). **(b)** Google image of Cayo Coco Lagoon. **(c)** View of the investigated lagoon with the various zones and the location of the sample, Core CC2. **(d)** Close view of the sample with the associated mineralogy, the two mineralising microbial mats are in red. The sample investigated here is sample M2.

Despite of the presence of calcium/magnesium carbonate in the microbial mats, they do display a high organic matter content. Different sources of organic matter (microbial mats, mangrove, soils and suspended particulate matter) were found throughout all of the depositional environment in Cayo Coco lagoon and their composition is fully described in Bouton *et al.* (2020). Sample M2 includes microbial biomass, as well as extracellular organic matter (EOM) forming an organic matrix. It is characterised by TOC (wt. %) between  $0.87 \pm 0.01$  and  $2.21 \pm 0.01$  depending on the studied fractions (0–200  $\mu\text{m}$  and 200–2000  $\mu\text{m}$ , respectively). The main contributor to the organic matter preserved within the sediment of the lagoons seem to be the slime (mostly composed of EOM) recognised in the permanently submersed zone. Nevertheless, the studied sample records  $\delta^{13}\text{C}_{\text{org}} = -16.44$  to  $-15.53$  ‰ (relative to VPDB), values comparable to the ones record in the mineralising microbial mats observed at surface all around the lagoonal networks (Bouton *et al.* 2020).

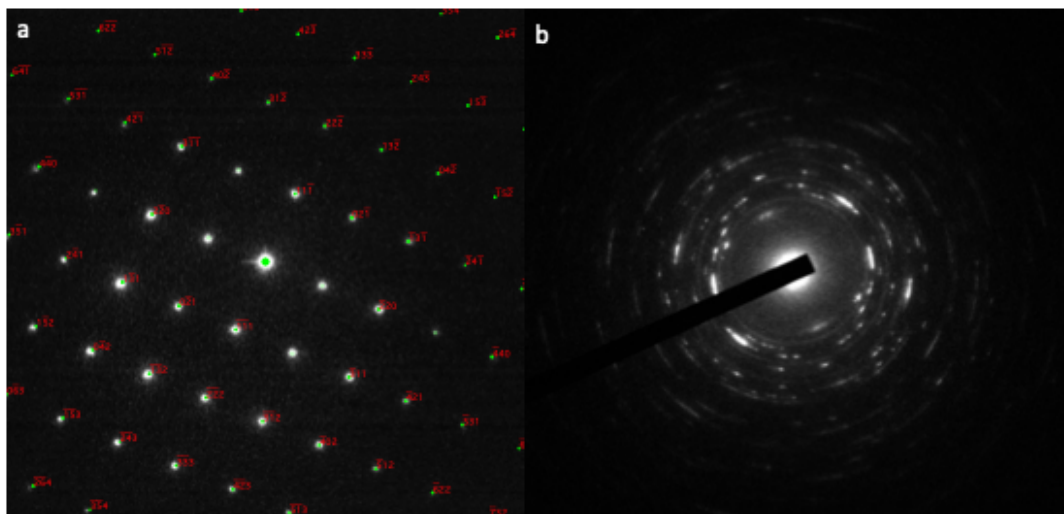
Molecular diversity studies of microbialites from Atexcac and Cayo Coco have highlighted the presence of diverse operational taxonomic units suggestive of sulfate reducing, sulfur oxidising, oxygenic and anoxygenic photosynthesising microorganisms (Pace *et al.*, 2018; Iniesto *et al.*, 2021). The floro-faunal content of these samples is both marine and continentally influenced, with foraminifera fragments, diatoms and few gastropods in Cayo Coco and predominantly diatoms in Atexcac.

## Methods

### SEM and TEM Analyses

Scanning Electron Microscopy (SEM) and Energy Dispersive X-ray Spectrometry (EDS) were used to characterise the microstructure and chemistry of pyrite and its inside inclusions for subsequent *in situ* extraction using focused ion beam milling (FIB). SEM observations were performed on a TESCAN VEGAII LSU at IMPMC with 15 kV accelerating voltage and a working distance of 15.4 mm according to the geometrical conditions required for EDS analyses on this microscope. SEM images were collected with both secondary (SE) and backscattered electrons (BSE) detectors. FIB ultrathin sections were extracted from different pyrite grains using an FEI Strata DB 235 at IEMN (Lille) This extraction procedure maintains textural integrity, and prevents shrinkage and deformation of microscale to nanoscale pores, even in the case of highly sensitive materials (Bassim *et al.*, 2014).

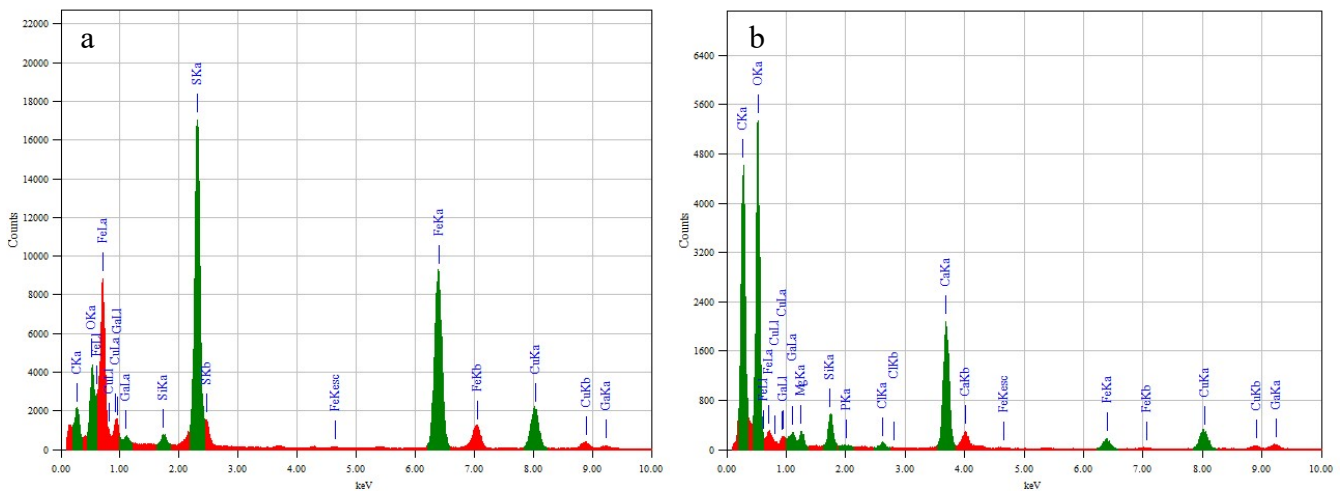
Transmission Electron Microscopy (TEM) analyses were performed on FIB sections to characterise crystallographic orientation and textures of the pyrites (Fig. S-3). TEM observations were performed with a JEOL 2100F Field Emission Gun (FEG) microscope (IMPMC, Paris, France) operating at 200 kV. Scanning Transmission Electron Microscopy (STEM) Z-contrast imaging was performed using the high-angle annular dark field (HAADF) mode. Selected-area diffraction (SAED) patterns were obtained on areas of interest (Fig. S-4).



**Figure S-3** (a) Indexed diffraction pattern of framboid pyrite from Cayo Coco. The diffraction pattern was indexed as pyrite seen along the [112] zone axis. Based on the extinction rule of the space group of pyrite (Pa-3), (1-10), (3-30), (20-1) are predicted to be extinct but can be detected because the grain was relatively thick and experienced double diffraction. (b) Selected area electron diffraction patterns of micropyrrite from Atexcac. The diffraction pattern is typical of polycrystalline nature of the micropyrrite. Different  $d$  spacings were measured and could be indexed as pyrite lattice planes as shown in Table S-1. The two rows of diffraction spots are at 90 °C with  $d$  spacings at  $\sim 3.12$  and  $3.82$  Å, indexed as (11-1) and (1-10), respectively.

**Table S-1** Pyrite  $d$  spacing ( $\text{\AA}$ ) and corresponding lattice planes.

$d$ spacing ( $\text{\AA}$ )	Interpreted pyrite lattice plane
3.13	(111)
2.71	(002)
2.45	(021)
2.24	(112)
1.93	(022)
1.65	(113)
1.52	(023)
1.47	(123)
1.35	(004)

**Figure S-4** STEM EDX analyses of sample from Cayo Coco. (a) EDX spectra indicate the presence of pyrites and (b) EDX spectra show the presence of the surrounding carbonate.

## Raman Spectroscopy

Raman spectroscopy was used to identify the carbonates (Fig. S-5). Raman data were collected using a Horiba Jobin Yvon LabRAM 800 HR spectrometer (UNIL, Lausanne, Switzerland) in a confocal configuration, equipped with an Ar<sup>+</sup> laser (532 nm) excitation source and an electron multiplying charge-coupled device (EMCCD). Measurements were performed at constant room temperature, directly on the sample surface, by focusing the laser beam with a 200  $\mu\text{m}$  confocal hole using a long working distance 50 $\times$  objective (NA = 0.70). This configuration provided a  $\sim 2$   $\mu\text{m}$  spot size for a laser power delivered at the sample surface below 1 mW. Light was dispersed using a 1800 gr/mm diffraction grating.

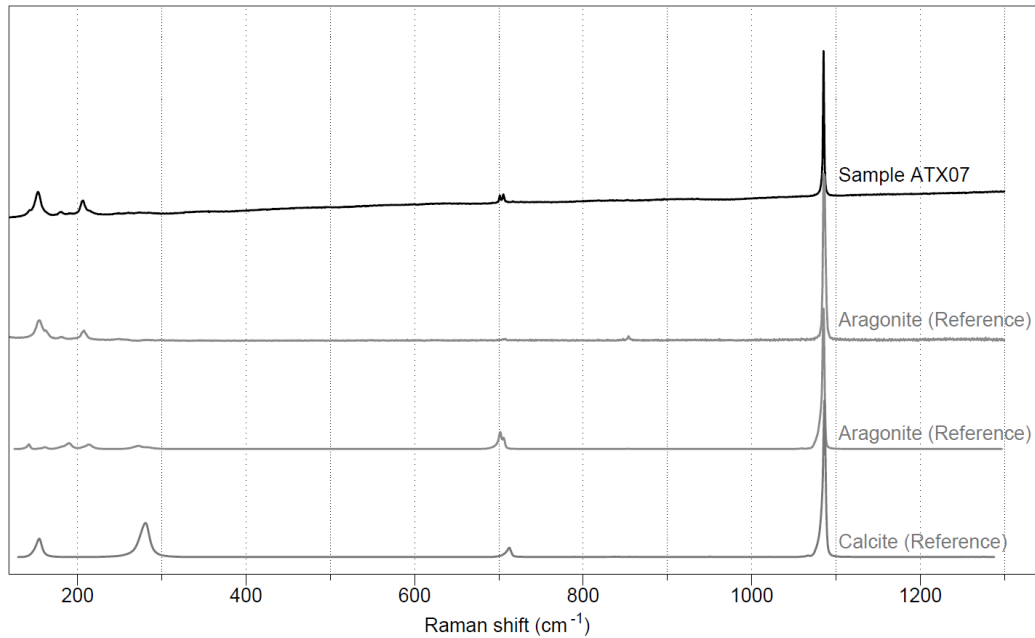


**Figure S-5** Representative Raman spectrum of carbonates in sample ATX07 (Atexcac) compared with two reference spectra of aragonite with different crystal orientations and calcite. Reference data are from the RRUFF database.

## Sulfur Isotope Analyses of Sulfate and Sulfide

### Sulfates

Lake Atexcac sulfate sulfur isotope composition has been measured using water samples collected at various depths across the chemocline of the lake in May 2019 (Table S-2). Water samples were filtered at 0.2  $\mu\text{m}$ . Dissolved sulfates were extracted after addition of a concentrated and acidic (1 M and  $\text{pH} \approx 2$ ) barium chloride salt solution to the samples and precipitation as barium sulfate (barite). Samples were acidified to a pH between 2 and 3 and reacted with the  $\text{BaCl}_2 \cdot \text{H}_2\text{O}$  solution for an hour at about 75  $^\circ\text{C}$  while being regularly agitated. Barite extracts were rinsed several times with deionised water, centrifuged and dried overnight at 50  $^\circ\text{C}$  in an oven. Sulfate recovery rates for all the samples were around 90 %, mostly due to loss of matter during scraping of  $\text{BaSO}_4$  from the glass tubes. Purity of the precipitates was also assessed through their concentration in S that were very close to that of pure international barite standard (NBS 127).

**Table S-2** Sulfate concentrations and isotope compositions of Lake Atexcac at 10 and 16 m depth.

Sample	$\delta^{34}\text{S}$		$\delta^{34}\text{S}_{\text{avg}}$ (‰)	$1\sigma$	$[\text{SO}_4^{2-}]$ mM
ATX-10 m	0.50	0.52	0.51	0.02	2.53
ATX-16 m	0.66	0.53	0.59	0.02	2.48

Sulfate from Cayo Coco lagoon waters was not directly analysed but its isotopic composition is considered to be similar to the canonical oceanic sulfate  $\delta^{34}\text{S}$ , *i.e.* around +21 ‰, since the lagoon is open and connected to the ocean at the locality of sampling (Babel and Schreiber, 2004). Average water composition is given in Table S-3. Water samples were analysed in the field for conductivity, pH, temperature and alkalinity. Conductivity was determined with a WTW Cond 3110 and a TetraCon 325 probe. pH was measured using a WTW pH 3110 with a Sentix 41 electrode or a Consort C561 pH-meter with a BioBlock Scientific electrode. The total alkalinity was assessed in the field using the Gran method. The alkalinity samples were filtered using 0.22- $\mu\text{m}$  polyethersulfone syringe filter. Water samples were stored

in glass vials (4-ml vials either under in situ pH conditions or acidified for analysis of major ions and 10-mL vials to determine the organic composition), kept refrigerated and transported to the laboratory. Major cation ( $\text{NH}_4^+$ ,  $\text{Na}^+$ ,  $\text{K}^+$ ,  $\text{Mg}^{2+}$ ,  $\text{Ca}^{2+}$ ) and anion ( $\text{Cl}^-$ ,  $\text{SO}_4^{2-}$ ,  $\text{NO}_3^-$  and  $\text{PO}_4^{3-}$ ) concentrations were determined by ion chromatography (Dionex DX-100 or ICS-1500, with an analytical precision of 0.2 mg/L) and dissolved organic carbon (DOC) content using a Shimadzu TOC-5000A analyser. Salinity values were calculated from conductivity and temperature values, according to the Aminot and Kerouel method (Aminot and K  rouel, 2004).

**Table S-3** Average water composition of Cayo Coco Lagoon.

	Conductivity (mS/cm)	pH	T (��C)	Alkalinity (mg/L) <i>in situ</i>	Na <sup>+</sup> (mg/L)	Mg <sup>2+</sup> (mg/L)	K <sup>+</sup> (mg/L)	Ca <sup>2+</sup> (mg/L)	Cl <sup>-</sup> (mg/L)	SO <sub>4</sub> <sup>2-</sup> (mg/L)
July 2014 (Average)	95.25	8.9	33	132.9	23	2,341	934	801.00	41,657	6,039

### Sulfides

A two-step extraction scheme was applied to retrieve both acid-volatile sulfide (AVS, mostly FeS) and chromium-reducible sulfide (CRS, mostly FeS<sub>2</sub>) from microbialites samples following Gr  ger *et al.* (2009). In short, agitated powdered samples diluted in ethanol reacted with cold 12M HCl for 2 h in order to liberate AVS. If any, resulting hydrogen sulfide was precipitated as Ag<sub>2</sub>S in a 0.3 M AgNO<sub>3</sub> solution. Then, a 1 M CrCl<sub>2</sub> solution (Canfield *et al.*, 1986; Gr  ger *et al.*, 2009) was added and reacted for another 2 h to liberate CRS, which in turn resulted in the precipitation of hydrogen sulfide as Ag<sub>2</sub>S. After centrifugation, silver sulfide precipitates were rinsed several times with deionised water and dried at 50   C for 48 h in an oven.

### Isotopic measurements

Both sulfides and sulfates  $\delta^{34}\text{S}$  measurements were performed at the Biog  osciences Laboratory of the Universit   de Bourgogne in Dijon, France. They were analysed on SO<sub>2</sub> molecules via combustion of 250–500   g of Ag<sub>2</sub>S and BaSO<sub>4</sub>, mixed with tungsten trioxide powder in equal amount to optimise sulfur oxidation during combustion, using a Vario PYRO cube (Elementar GmbH) connected online via an open split device to an IsoPrime IRMS system. International standards (IAEA-S1/-S2/-S3 and -NBS 127 for Ag<sub>2</sub>S and BaSO<sub>4</sub>, respectively) were used for calibration. Results are reported in delta notation against the Vienna Canyon Diablo Troilite standard (VCDT). All measurements were duplicated. Standard and BaSO<sub>4</sub> samples reproducibility is better than  $\pm 0.1$  ‰ (1  ).

Waters from the surface to the chemocline in Atexcac (~20–25 m depth) show relatively homogeneous  $\delta^{34}\text{S}$ , around  $0.6 \pm 0.1$  ‰ ( $n = 2$ ). Bulk solid sulfide  $\delta^{34}\text{S}$  of the Atexcac microbialite has a mean value of  $-28.73 \pm 0.3$  ‰ ( $n = 2$ ), consisting almost exclusively of CRS.

### Sulfur Isotope Analyses by NanoSIMS

Samples embedded in epoxy were polished down to 0.25 mm and gold coated. The data we report in this study were collected during three different analytical sessions, in May 2017 at IMPMC, November 2018 and October 2019 at EPFL, using the same methodology. Secondary ions of <sup>12</sup>C<sup>14</sup>N<sup>-</sup>, <sup>32</sup>S<sup>-</sup> and <sup>34</sup>S<sup>-</sup> were simultaneously measured in multicollection mode using electron multipliers (EM) with a dead time of 44 ns. The mass resolving power was set to 18,000 (Cameca definition) to resolve potential interferences on masses 32 and 34. To avoid the build-up of positive charges over the sample's surface, an electron flood gun was used. Each analysis was preceded by a 15 min pre-sputtering phase using a 0.5 nA primary Cs<sup>+</sup> beam scanned over an area slightly larger than the area of interest (25 × 25   m) to locally remove the gold coating and surface contamination, and to reach steady state sputtering regime. 20 × 20   m images of the areas of interest were collected using a 0.8 pA Cs<sup>+</sup> primary beam with a 120 nm probe size, using a 256 × 256 pixels resolution, a dwell time of 1 ms/pixel and 60 cycles were stacked to get decent counting statistic.



As already described in Marin-Carbonne *et al.* (2018), S isotope analysis in sulfides is known to be biased by quasi simultaneous arrival (QSA) effect on the EM (Slodzian *et al.*, 2004). The correction of this effect was achieved by applying the method described by Nishizawa *et al.* (2010). Using different aperture slits to produce variations of the secondary ion signal over primary current ratio on the standard, we determined a QSA correcting factor of 0.54 and 0.66 for  $^{34}\text{S}/^{32}\text{S}$  ratio for each sessions consistent with the value of 0.69 previously published (Slodzian *et al.*, 2004; Bontognali *et al.*, 2012; Marin-Carbonne *et al.*, 2018).

Two different pyrite standards (Maine,  $\delta^{34}\text{S} = -20.62 \pm 0.01$  ‰, and CAR 123,  $\delta^{34}\text{S} = +1.5 \pm 0.01$  ‰) were analysed in order to determine QSA correcting factors and instrumental mass fractionation (see Table S-4 for two sessions). Standards were analysed at the beginning and end of the sessions and every day for assessing the stability of the instruments.

NanoSIMS images were processed by LIMAGE© software from Larry Nittler (Carnegie Institution, Washington, DC). After applying regular deadtime correction (44 ns), the different frames (one frame per cycle) were aligned and region of interest (ROIs) corresponding to each framboidal pyrite were defined using the particle definition mode. The size of ROIs ranges from 1 to 270  $\mu\text{m}^2$ . Total counts were then extracted and QSA and IMF corrections were applied in Table S-5.  $\delta^{34}\text{S}$  values *versus* Vienna Canyon Diablo Troilite (V-CDT) were calculated for each framboidal pyrite.

**Table S-4** Measured  $^{34}\text{S}/^{32}\text{S}$  ratios and  $\delta^{34}\text{S}$  values corrected from QSA effect in two different sessions for the Maine and UCLA pyrite standards. Instrumental mass fractionation was 1.024 in the first session and 1.0159 in the second.

Standards	$\delta^{34}\text{S}$ true (‰)	$^{34}\text{S}/^{32}\text{S}$ true	$^{34}\text{S}/^{32}\text{S}$ measured	1 $\sigma$	$\delta^{34}\text{S}$ corr QSA (‰)
<i>Session 1</i>					
UCLA	1.5	0.04423001	0.045594	1.47E-04	32.4
MAINE	-20.1	0.04327607	0.044599	7.24799E-05	9.9
<i>Session 2</i>					
UCLA	1.5	0.04423001	0.045219	6.25133E-05	23.9
MAINE	-20.1	0.04327607	0.044263	1.14E-04	2.2

**Table S-5** Sulfur isotope compositions of framboidal and micropyrates.

Table S-5 is available for download (Excel) from the online version of the article at <https://doi.org/10.7185/geochemlet.2209>.

The studied framboidal pyrites consist of between 240 and 498 different pyrite grains. For four framboidal pyrites, we defined ROIs for each individual grain inside the framboidal pyrite and extracted the total counts and calculated the isotope ratios. Some of them were quite small with low total counts, therefore the associated error, influenced by counting statistics, is large. S isotope compositions are compared to framboid size or micropyrates grain size in Figures S-6 and S-7, respectively, and to C/N count rates in Figure S-8.



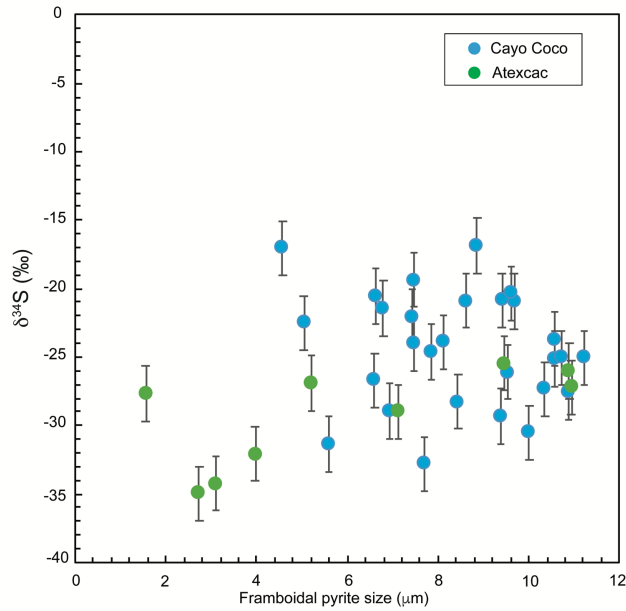


**Figure S-6** Sulfur isotope composition and framboid size for Cayo Coco and Atexcac pyrites.

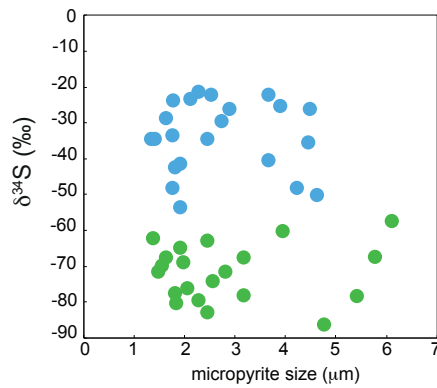


**Figure S-7** δ<sup>34</sup>S values *versus* size for micropyrite in Cayo Coco (blue) and Atexcac (green). Error bars on the δ<sup>34</sup>S values are within the symbol size.

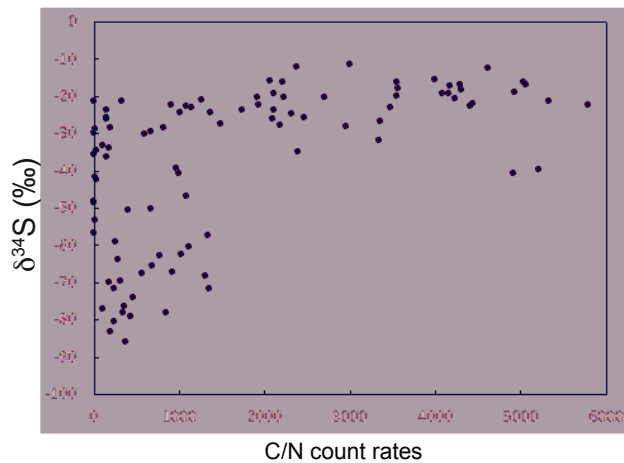


**Figure S-8** δ<sup>34</sup>S values *versus* C/N ratio count rates. The error bars on the δ<sup>34</sup>S values are within the symbol size.

## Framboidal Pyrites

Framboids are only found in surface unconsolidated sediment or enclosed within foraminifera tests. By contrast, micropyrite grains are either disseminated or aligned within microbialite laminae, in close association with aragonite and Mg-rich silicate phases (Fig. 1). Framboidal pyrites aggregate a mixture of euhedral, rounded and pyramidal pyrite grains (Fig. 1a–b), while micropyrites are predominantly euhedral (Fig. 1c–d). Transmission electron microscopy analyses show that micropyrites are composed of nanocrystals with various orientations, while framboidal pyrites are composed of micrometric pyrite crystals (Fig. 2). Framboidal pyrites are surrounded by a layer of iron oxide (Fig. 2), suggesting late oxidation (Maclean *et al.*, 2008). Micropyrites are surrounded by external layers of Fe-Mg silicate (Atexcac) or amorphous silica (Cayo Coco, Fig. 2), suggesting fluid induced reaction between pyrite and Mg authigenic silicates during or after biomineralisation and/or lithification. Previous investigations have shown that the hydrated Mg-silicate rich phase, identified as kerolite in Atexcac, is tightly linked to an early mineralisation step of microbialites (Zeyen *et al.*, 2015; Bouton *et al.*, 2016; Pace *et al.*, 2018). We suggest that the presence of the Mg-silicate rich phase associated with sulfide provide evidences for an early syngenetic origin of the micropyrite grains.

Framboidal pyrites display homogeneous sizes in both samples (Fig. S-9), consistent with a synsedimentary origin (Maclean *et al.*, 2008).

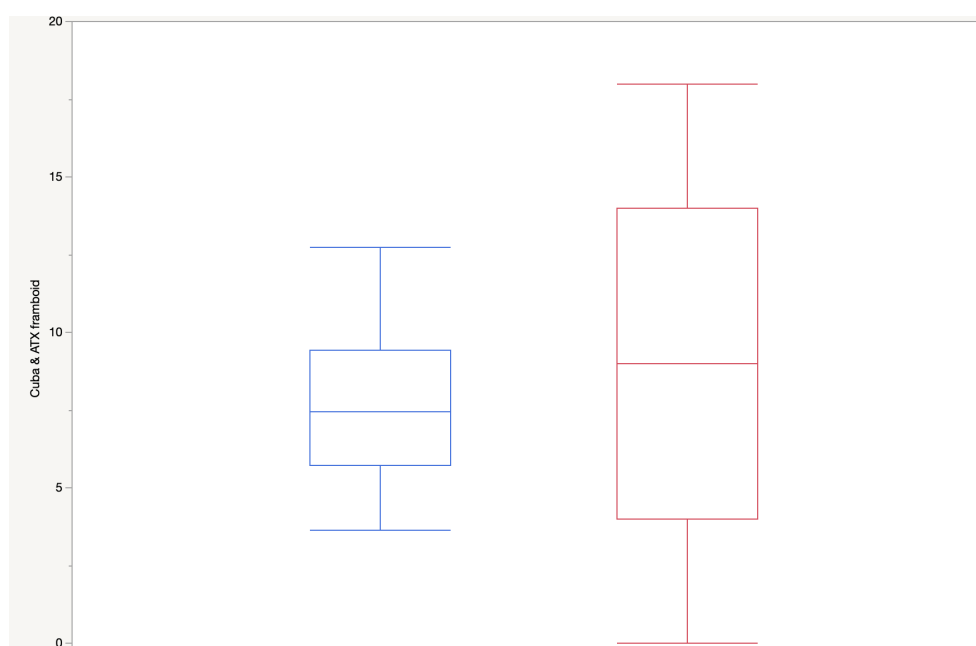


**Figure S-9** Size distribution (in  $\mu\text{m}$ ) of framboidal pyrite from Cayo Coco (blue) and Atexcac (red). The average sizes are  $7.6 \pm 2.9 \mu\text{m}$  and  $7.4 \pm 4.8 \mu\text{m}$  for Cayo Coco and Atexcac, respectively.

In detail, however, the number of crystallites inside each framboidal strongly varies (between 40 to more than 300) and exceeds previous reports giving an upper limit of 100 for framboidal crystallites precipitating within microbial mats (Popa *et al.*, 2004). Framboidal pyrite size has been used to infer the oxygenation state of their depositional environment, where pyrites precipitating in sediments overlain by an oxic water column display larger sizes ( $>10 \mu\text{m}$ ) than the ones precipitated under euxinic conditions (Wilkin *et al.*, 1996). The small ( $<10 \mu\text{m}$ ) and homogeneous size of framboidal pyrites reported here challenges the locus-size hypothesis since both samples have been formed in fully oxygenated aqueous solutions (Fig. S-10).

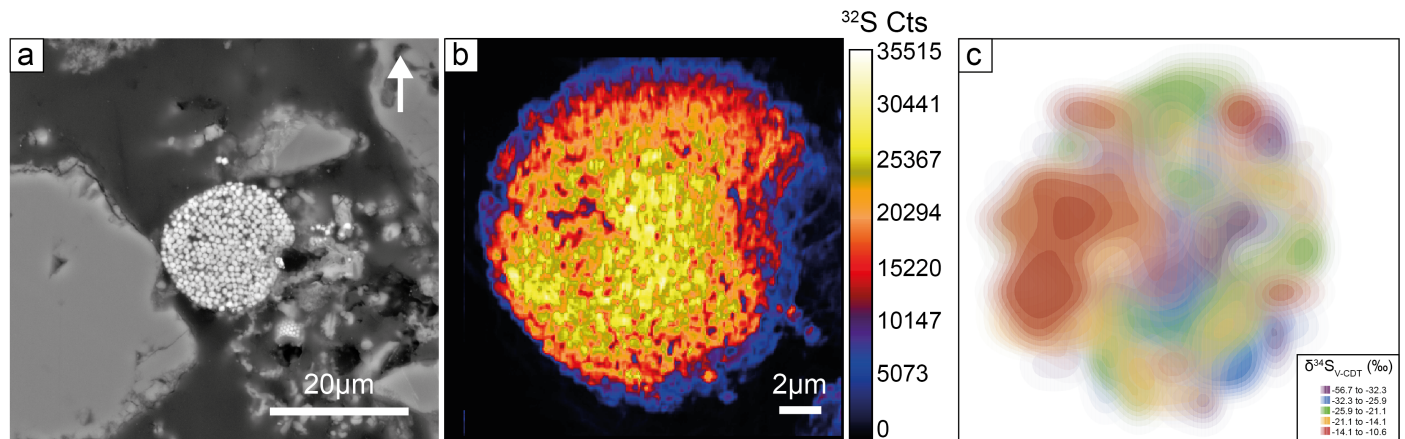


**Figure S-10** SEM and NanoSIMS count rate images of framboidal pyrite from Atexcac showing heterogeneous  $\delta^{34}\text{S}$  distribution. The top of the mat is indicated by the arrow. In this case, the gradient is not very visible.

## Supplementary Information References

- Aminot, A., K erouel, R. (2004) Dissolved organic carbon, nitrogen and phosphorus in the NE Atlantic and the NW Mediterranean with particular reference to non-refractory fractions and degradation. *Deep Sea Research Part I: Oceanographic Research Papers* 51, 1975–1999. <https://doi.org/10.1016/j.dsr.2004.07.016>
- Bassim, N., Scott, K., Giannuzzi, L.A. (2014) Recent advances in focused ion beam technology and applications. *MRS Bulletin* 39, 317–325. <https://doi.org/10.1557/mrs.2014.52>
- Bontognali, T.R.R., Sessions, A.L., Allwood, A.C., Fischer, W.W., Grotzinger, J.P., Summons, R.E., Eiler, J.M. (2012) Sulfur isotopes of organic matter preserved in 3.45-billion-year-old stromatolites reveal microbial metabolism. *Proceedings of the National Academy of Sciences* 109, 15146–15151. <https://doi.org/10.1073/pnas.1207491109>
- Bouton, A., Vennin, E., Pace, A., Bourillot, R., Dupraz, C., Thomazo, C., Brayard, A., D esaubliaux, G., Visscher, P.T. (2016) External controls on the distribution, fabrics and mineralization of modern microbial mats in a coastal hypersaline lagoon, Cayo Coco (Cuba). *Sedimentology* 63, 972–1016. <https://doi.org/10.1111/sed.12246>
- Bouton, A., Vennin, E., Thomazo, C., Mathieu, O., Garcia, F., Jaubert, M., Visscher, P. (2020) Microbial Origin of the Organic Matter Preserved in the Cayo Coco Lagoonal Network, Cuba. *Minerals* 10, 143. <https://doi.org/10.3390/min10020143>
- Canfield, D.E., Raiswell, R., Westrich, J.T., Reaves, C.M., Berner, R.A. (1986) The use of chromium reduction in the analysis of reduced inorganic sulfur in sediments and shales. *Chemical Geology* 54, 149–155. [https://doi.org/10.1016/0009-2541\(86\)90078-1](https://doi.org/10.1016/0009-2541(86)90078-1)
- Cepero, E., Lawrence, A. (2006) Before and After the Cayo Coco Causeway, Cuba: A Critical View From Space. *Cuba in Transition* 16, 212–220.
- Ferrari, L., Orozco-Esquivel, T., Manea, V., Manea, M. (2012) The dynamic history of the Trans-Mexican Volcanic Belt and the Mexico subduction zone. *Tectonophysics* 522–523, 122–149. <https://doi.org/10.1016/j.tecto.2011.09.018>
- Gonzalez-De Zayas, R., Merino-Ibarra, M. (2010) Water, salt and nutrients budgets in Larga Lagoon, Cayo Coco, Cuba. *Land–Ocean Interactions in the Coastal Zone (LOICZ)*, 12 p, 12 p. <https://doi.org/10.13140/RG.2.1.1589.4569>
- Gr oger, J., Franke, J., Hamer, K., Schulz, H.D. (2009) Quantitative recovery of elemental sulfur and improved selectivity in a chromium-reducible sulfur distillation. *Geostandards and Geoanalytical Research* 33, 17–27. <https://doi.org/10.1111/j.1751-908X.2009.00922.x>
- Iniesto, M., Moreira, D., Reboul, G., Deschamps, P., Benzerara, K., Bertolino, P., Sagh ai, A., Tavera, R., L opez-Garc a, P. (2021) Core microbial communities of lacustrine microbialites sampled along an alkalinity gradient. *Environmental Microbiology* 23, 51–68. <https://doi.org/10.1111/1462-2920.15252>
- MacLean, L.C.W., Tyliszczak, T., Gilbert, P.U.P.A., Zhou, D., Pray, T.J., Onstott, T.C., Southam, G. (2008) A high-resolution chemical and structural study of framboidal pyrite formed within a low-temperature bacterial biofilm. *Geobiology* 6, 471–480. <https://doi.org/10.1111/j.1472-4669.2008.00174.x>
- Marin-Carbonne, J., Remusat, L., Sforza, M.C., Thomazo, C., Cartigny, P., Philippot, P. (2018) Sulfur isotope’s signal of nanopyrates enclosed in 2.7 Ga stromatolitic organic remains reveal microbial sulfate reduction. *Geobiology* 16, 121–138. <https://doi.org/10.1111/gbi.12275>
- Nishizawa, M., Maruyama, S., Urabe, T., Takahata, N., Sano, Y., (2010) Micro-scale (1.5  $\mu\text{m}$ ) sulphur isotope analysis of contemporary and early Archean pyrite. *Rapid Communications in Mass Spectrometry* 24, 1397–1404. <https://doi.org/10.1002/rcm.4517>

- Pace, A., Bourillot, R., Bouton, A., Vennin, E., Braissant, O., Dupraz, C., Duteil, T., Bundeleva, I., Patrier, P., Galaup, S., Yokoyama, Y., Franceschi, M., Virgone, A., Visscher, P.T. (2018) Formation of stromatolite lamina at the interface of oxygenic-anoxygenic photosynthesis. *Geobiology* 16, 378–398. <https://doi.org/10.1111/gbi.12281>
- Popa, R., Kinkle, B.K., Badescu, A. (2004) Pyrite framboids as biomarkers for iron-sulfur systems. *Geomicrobiology Journal* 21, 193–206. <https://doi.org/10.1080/01490450490275497>
- Sigala, I., Caballero, M., Correa-Metrio, A., Lozano-García, S., Vázquez, G., Pérez, L., Zawisza, E. (2017) Basic limnology of 30 continental waterbodies of the Transmexican Volcanic Belt across climatic and environmental gradients. *Boletín de la Sociedad Geológica Mexicana* 69, 313–370. <https://doi.org/10.18268/BSGM2017v69n2a3>
- Slodzian, G., Hillion, F., Stadermann, F.J., Zinner, E. (2004) QSA influences on isotopic ratio measurements. *Applied Surface Science* 231–232, 874–877. <https://doi.org/10.1016/j.apsusc.2004.03.155>
- Wilkin, R.T., Barnes, H.L., Brantley, S.L. (1996) The size distribution of framboidal pyrite in modern sediments: An indicator of redox conditions. *Geochimica et Cosmochimica Acta* 60, 3897–3912. [https://doi.org/10.1016/0016-7037\(96\)00209-8](https://doi.org/10.1016/0016-7037(96)00209-8)
- Zeyen, N., Benzerara, K., Li, J., Groleau, A., Balan, E., Robert, J.-L., Estève, I., Tavera, R., Moreira, D., López-García, P. (2015) Formation of low-T hydrated silicates in modern microbialites from Mexico and implications for microbial fossilization. *Frontiers in Earth Science* 3, 64. <https://doi.org/10.3389/feart.2015.00064>
- Zeyen, N., Benzerara, K., Beyssac, O., Daval, D., Muller, E., Thomazo, C., Tavera, R., López-García, P., Moreira, D., Duprat, E. (2021) Integrative analysis of the mineralogical and chemical composition of modern microbialites from ten Mexican lakes: What do we learn about their formation? *Geochimica et Cosmochimica Acta* 305, 148–184. <https://doi.org/10.1016/j.gca.2021.04.030>